Tunneling Magnetoresistance Devices Based on Topological Insulators: Ferromagnet–Insulator–Topological-Insulator Junctions Employing Bi$_2$Se$_3$

Matthias Götte, Tomi Paananen, Günter Reiss, and Thomas Dahm

Universität Bielefeld, Fakultät für Physik, Postfach 100131, D-33501 Bielefeld, Germany
(Received 11 July 2014; revised manuscript received 24 September 2014; published 17 November 2014)

We theoretically investigate tunneling magnetoresistance (TMR) devices, which are probing the spin-momentum coupled nature of surface states of the three-dimensional topological insulator Bi$_2$Se$_3$. Theoretical calculations are performed based on a realistic tight-binding model for Bi$_2$Se$_3$. We study both three-dimensional devices, which exploit the surface states of Bi$_2$Se$_3$, as well as two-dimensional devices, which exploit the edge states of thin Bi$_2$Se$_3$ strips. We demonstrate that the material properties of Bi$_2$Se$_3$ allow a TMR ratio at room temperature of the order of 1000%. Analytical formulas are derived that allow a quick estimate of the achievable TMR ratio in these devices. The devices can be used to measure the spin polarization of the topological surface states as an alternative to spin ARPES. Unlike TMR devices based on magnetic tunnel junctions the present devices avoid the use of a second ferromagnetic electrode whose magnetization needs to be pinned.

I. INTRODUCTION

Topological insulators (TI) are materials which possess an insulating gap in the bulk but conducting states at the surface. These surface states are protected by the topological properties of the material and are robust against time-reversal-symmetric perturbations such as nonmagnetic impurities, for example. After first being predicted theoretically [1,2], subsequently several materials have been confirmed to be topological insulators experimentally [3–9]. Because of spin-orbit coupling the momentum of the surface states is locked with the spin of the electrons, which means that electrons with opposite spin propagate into the opposite direction. [9–12]. The robustness of the surface states against back-scattering promises long spin-diffusion lengths. These features make topological insulators particularly interesting for applications in spintronics [13–24]. In addition, spin-dependent tunneling into the surface states opens a way to investigate their properties such as spin polarization.

In the present work we theoretically study different arrangements to realize a tunneling magnetoresistance (TMR) device using a ferromagnet coupled via a tunnel barrier to a topological insulator. In contrast to conventional TMR junctions such a device does not need a second ferromagnetic layer, because the spin locking in the topological insulator already provides an intrinsic magnetic reference. Additionally, the device can be used to probe the spin-locked surface states in the TI. We will show that the material properties of the topological insulator determine the maximum TMR ratio that can be achieved. Specifically, we will present calculations for the three-dimensional topological insulator Bi$_2$Se$_3$, which has been studied well in the past both theoretically and experimentally [6,25–28]. This material is particularly interesting due

to its comparatively large band gap of about 0.3 eV. As we will see, this property allows us to achieve large TMR ratios already at room temperature.

II. MODEL

For our calculations we use a realistic tight-binding model for Bi$_2$Se$_3$ that has been derived from band-structure calculations by Liu *et al.* [28] based on $\mathbf{k} \cdot \mathbf{p}$ theory. The Hamiltonian takes into account two orbitals at each lattice site and reads

$$H(\mathbf{k}) = \epsilon_0(\mathbf{k})\mathbb{1}_{4\times4} + \sum_{i=1}^{4} m_i(\mathbf{k})\Gamma^i + \mathcal{R}_1(\mathbf{k})\Gamma^5 + \mathcal{R}_2(\mathbf{k})\Gamma^3. \tag{1}$$

Here,

$$\epsilon_0(\mathbf{k}) = C_0 + 2C_1(1 - \cos k_z)$$
$$+ \frac{4}{3}C_2\left(3 - 2\cos\frac{1}{2}k_x\cos\frac{\sqrt{3}}{2}k_y - \cos k_x\right),$$

$$m_1(\mathbf{k}) = A_0\frac{2}{\sqrt{3}}\cos\frac{1}{2}k_x\sin\frac{\sqrt{3}}{2}k_y,$$

$$m_2(\mathbf{k}) = -A_0\frac{2}{3}\left(\sin\frac{1}{2}k_x\cos\frac{\sqrt{3}}{2}k_y + \sin k_x\right),$$

$$m_3(\mathbf{k}) = B_0\sin k_z,$$

$$m_4(\mathbf{k}) = M_0 + 2M_1(1 - \cos k_z)$$
$$+ \frac{4}{3}M_2\left(3 - 2\cos\frac{1}{2}k_x\cos\frac{\sqrt{3}}{2}k_y - \cos k_x\right)$$

are tight-binding parameters defined on a bilayer hexagonal lattice following Hao and Lee [29]. The terms

$$\mathcal{R}_1(\mathbf{k}) = 2R_1(\cos\sqrt{3}k_y - \cos k_x)\sin k_x, \quad (2)$$

$$\mathcal{R}_2(\mathbf{k}) = \frac{16}{3\sqrt{3}}R_2\left(\cos\frac{\sqrt{3}}{2}k_y - \cos\frac{3}{2}k_x\right)\sin\frac{\sqrt{3}}{2}k_y \quad (3)$$

are third-order terms to lowest order in momentum $\mathbf{k}$ [28]. The Dirac Γ matrices are represented by $\Gamma^{1,2,3,4,5} = (\tau_1 \otimes \sigma_1, \tau_1 \otimes \sigma_2, \tau_2 \otimes \mathbb{1}_{2\times2}, \tau_3 \otimes \mathbb{1}_{2\times2}, \tau_1 \otimes \sigma_3)$, where τ_i and σ_i are the Pauli matrices in the orbital and spin space, respectively. The model parameters are derived from Liu *et al.* [28] using the atomic distances $a = 4.14$ Å and $c = \frac{28.64}{15}$ Å (a and $15c$ are the lattice constants given in Refs. [30–32]; a unit cell consists of 15 layers in the c direction): $A_0 = 0.804$ eV, $B_0 = 1.184$ eV, $C_1 = 1.575$ eV, $C_2 = 1.774$ eV, $M_0 = -0.28$ eV, $M_1 = 1.882$ eV, $M_2 = 2.596$ eV, $R_1 = 0.713$ eV, and $R_2 = -1.597$ eV. C_0 is only a tiny energy shift and is chosen to be 0, which corresponds to undoped Bi_2Se_3. Here and in the following all energies are given with respect to the Fermi level of the topological insulator.

In Fig. 1 a tight-binding model of a ferromagnet–insulator–topological-insulator (F-I-TI) junction is shown. The topological insulator is modeled by the Hamiltonian equation (1), which we Fourier transform perpendicular to the junction plane into real space onto its lattice. For the in-plane directions we assume periodic boundary conditions, allowing us to keep the in-plane momentum components (e.g., k_x and k_y for a z surface) as good quantum numbers. The ferromagnet (FM) is modeled as a metal with two spin-split subbands. For that purpose we use the same Hamiltonian equation (1) with parameters $C_F \equiv C_1 = C_2 = 0.25$ eV and $A_0 = B_0 = M_0 = M_1 = M_2 = R_1 = R_2 = 0$ corresponding to a 3 eV bandwidth. Additionally, we add an exchange field of strength W of the form

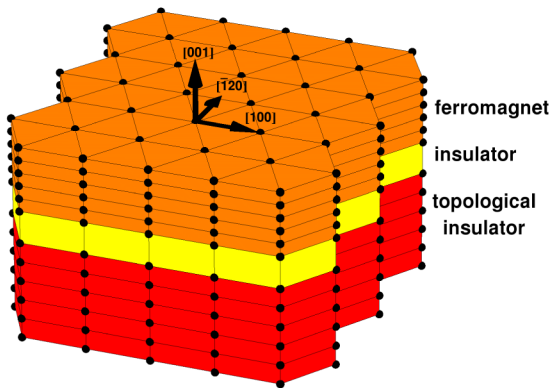$$H_{\text{ex}} = -W\mathbb{1}_{2\times2} \otimes (\mathbf{n} \cdot \vec{\sigma}), \quad (4)$$

FIG. 1. Tight-binding model of a ferromagnet–insulator–topological-insulator (F-I-TI) junction with the ferromagnet on the [001] surface of the topological insulator, corresponding to setup A and B in Fig. 2.

with $\mathbf{n} = (\sin\theta_F\cos\varphi_F, \sin\theta_F\sin\varphi_F, \cos\theta_F)$ and $\vec{\sigma} = (\sigma_1, \sigma_2, \sigma_3)$, which can be polarized in arbitrary direction $\mathbf{n}$. Choosing $W = 0.5$ eV, states with one spin orientation reside at the Fermi surface, while those with opposite orientation are shifted to higher energies. This choice corresponds to a 100% spin polarization of the ferromagnet. A reduced spin polarization of the ferromagnet is handled by a superposition of two calculations with opposite polarity of the exchange field, as discussed in the Appendix. The insulating barrier is modeled by a tunneling Hamiltonian of the form

$$H_T = -C_B \sum_{k_x,k_y,\alpha,\sigma} d^\dagger_{k_x,k_y,\alpha,\sigma} c_{k_x,k_y,\alpha,\sigma} + \text{H.c.}, \quad (5)$$

where $d^\dagger_{k_x,k_y,\alpha,\sigma}$ creates an electron in orbital α with spin σ in the top layer of the topological insulator and $c_{k_x,k_y,\alpha,\sigma}$ destroys an electron in the bottom layer of the ferromagnet. Here, k_x and k_y are the momentum components perpendicular to the junction plane. For the numerical calculations we choose a small hopping matrix element of $C_B = 0.1$ eV, however, the relative TMR values calculated below do not depend on this choice.

Because of the structure of the Hamiltonian equation (1), topological surface states appear on the topological-insulator side of the junction. The dispersion of the surface states forms a Dirac cone, which is hexagonally warped due to the third-order terms, Eqs. (2) and (3) [33]. Note that the position of the Dirac point and the shape of the Dirac cone depends on the surface direction. The surface states are spin polarized with the direction of the spin helically winding around the Dirac cone. The spin-polarized tunneling current through the barrier thus flows off into different directions in the topological insulator depending on the polarization of the ferromagnet. In particular, the direction of the current in the topological insulator can be controlled by rotation of the exchange field in the ferromagnet. This effect can be used to construct a TMR device from such a junction.

Possible setups for such devices are shown in Fig. 2. The spin-polarized current that is injected via a ferromagnetic electrode (denoted by FM in Fig. 2) into the topological surface states can be extracted through metallic electrodes (M) at opposite positions on the same surface. For a given bias voltage the current through the two metallic electrodes will differ in strength due to the spin-momentum locking of the surface states. This difference leads to different resistances with respect to the ferromagnetic electrode, because the spin direction of the tunneling electrons will favor current flow to one of the two metallic electrodes. The resistances will vary with the direction of the exchange field in the ferromagnet resulting in a directional dependence of the resistance on the magnetization, i.e., a TMR effect. Because of the anisotropy of Bi_2Se_3 we study six
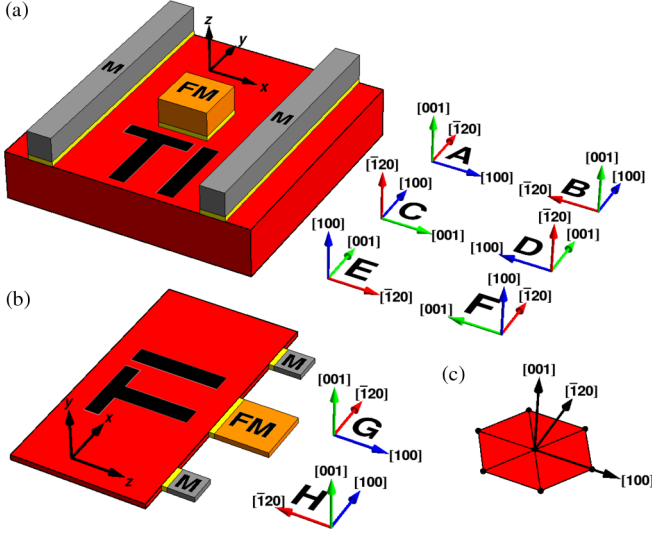
FIG. 2. Setups for TMR devices studied in this work. Different orientations of the crystal axes of the TI relative to the electrodes are given by the coordinate systems A–H, (a) for a three-dimensional TI and (b) for a two-dimensional TI. In (c) the crystallographic directions of the TI are shown.

setups for a three-dimensional (3D) device (A–F) and two for a two-dimensional (2D) device (G, H) as shown in Fig. 2, which may yield different TMR ratios. These setups differ in the crystallographic orientation of the topological insulator relative to the junction plane. In the 3D cases we investigate the three clean surfaces in the [001], [100], and [$\bar{1}$20] direction with two orthogonal arrangements of the metallic electrodes each. The 2D case could be realized by a thin film strip contacted at the edges, i.e., with an experimentally more complex arrangement. For that purpose, the film thickness should be less than 6 nm (6 quintuple layers) in order to ensure that the top and bottom surface states become sufficiently hybridized [34]. On the other hand, the film thickness should be at least 1.5 nm to avoid having the material become topologically trivial [35]. Here, we consider a film thickness of 3 nm to stay within these two limits. In this case, the parameter M_0 needs to be reduced to an effective 2D value of $M_0 = -0.197$ eV, as has been discussed in Ref. [35]. In the 2D case we do not consider thin films grown along the [100] or [$\bar{1}$20] direction, as these are technically difficult to realize. In the following, the Cartesian coordinates (x, y, z) are tied to the geometry of the devices, while the orientation of the crystal in these devices is expressed by Miller indices, as indicated in Fig. 2. Hence, k_z is always the momentum perpendicular to the surface plane and k_x and k_y are the in-plane momenta with k_x pointing from the junction towards the metallic electrode. Note that this definition of the Cartesian coordinates only in the case of setup A coincides with that in Eqs. (1) and (4).

The tunneling current through the insulating barrier is calculated using Fermi's golden rule

$$\Gamma_{mn} = \frac{2\pi}{\hbar} \delta(E_n - E_m)|\langle n|H_T|m\rangle|^2, \tag{6}$$

which gives the transition rate from an initial state $|m\rangle$ into a final state $|n\rangle$. Here, H_T is the tunneling Hamiltonian equation (5) of the insulating barrier [36]. For a given bias voltage U between the ferromagnetic electrode and the topological insulator, the total tunneling current is given by the expression [37]

$$I(U) = \frac{2\pi e}{\hbar} \sum_{m,n} [f(E_m - eU) - f(E_n)]|\langle n|H_T|m\rangle|^2$$
$$\times \delta(E_n - E_m). \tag{7}$$

Here, the sum runs over all eigenstates m and n of the ferromagnet and the topological insulator. The Fermi function

$$f(E) = \frac{1}{1 + e^{E/k_B T}} \tag{8}$$

takes into account the occupation of the eigenstates at finite temperature. Differentiating I with respect to U leads to the differential conductance

$$G(U) = \frac{dI}{dU} = \frac{\pi e^2}{2\hbar k_B T} \sum_{m,n} \frac{1}{\cosh^2 \frac{E_m - eU}{2k_B T}} |\langle n|H_T|m\rangle|^2$$
$$\times \delta(E_n - E_m), \tag{9}$$

which is used to define the TMR ratio

$$\text{TMR}(U, \theta_F, \varphi_F) = \frac{G_{\max}(U) - G(U, \theta_F, \varphi_F)}{G(U, \theta_F, \varphi_F)}. \tag{10}$$

Here, θ_F and φ_F define the direction of the exchange field equation (4), and $G_{\max}(U)$ is the maximal differential conductance with respect to one metallic electrode obtained when the exchange field and the polarization of the surface electrons with propagation direction perpendicular to that electrode are parallel. The maximal TMR ratio can then be obtained by rotating the exchange field by π into the antiparallel orientation or, because of the spin-momentum locking of the TI surface states, by comparing the differential conductances with respect to both metallic electrodes (see Fig. 2). To calculate the differential conductance with respect to the different metallic electrodes, we sum only over those eigenstates of the TI with a positive group-velocity component $v_x = \frac{1}{\hbar} \frac{\partial E}{\partial k_x}$ in the direction of the electrodes for one electrode and over those with a negative group-velocity component for the opposite electrode.

III. RESULTS

In this section we present our results for the TMR ratio in Bi$_2$Se$_3$ based on numerical calculations as well as an analytical approximation. The analytical approximation is derived in the Appendix. It assumes isotropic helical

surface states and neglects the influence of bulk states. This should be a good approximation for bias voltages chosen within the bulk gap of the material in the vicinity of the Dirac point. While the numerical calculations give an exact solution based on the Hamiltonian equation (1) including the influence of the bulk states, the analytical approximation gives a formula depending on the spin polarization p of the topological surface states. Here, $0 \leq p \leq 1$ is the average magnitude of the spin-expectation value in the vicinity of the Dirac point. The analytical formula is useful, as it provides a quick estimate of the TMR ratio and can be used for different materials once the spin polarization p of the surface states is known. Depending on the dimensionality of the device the formulas for the TMR ratio are slightly different, but independent of temperature and bias voltage (see the Appendix):

$$\text{TMR}_{3D}(p, q, \varphi_F) = \frac{1 + \sin\varphi_F}{\frac{\pi}{2pq} - \sin\varphi_F}, \qquad (11)$$

$$\text{TMR}_{2D}(p, q, \varphi_F) = \frac{1 + \sin\varphi_F}{\frac{1}{pq} - \sin\varphi_F}. \qquad (12)$$

Here, $0 \leq q \leq 1$ is the spin polarization of the ferromagnet. The angle φ_F is the in-plane polarization angle of the exchange field. The maximal TMR ratio is reached after a π rotation of the exchange field ($\varphi_F = \frac{\pi}{2}$) and is shown as a function of pq in Fig. 3. It is limited to
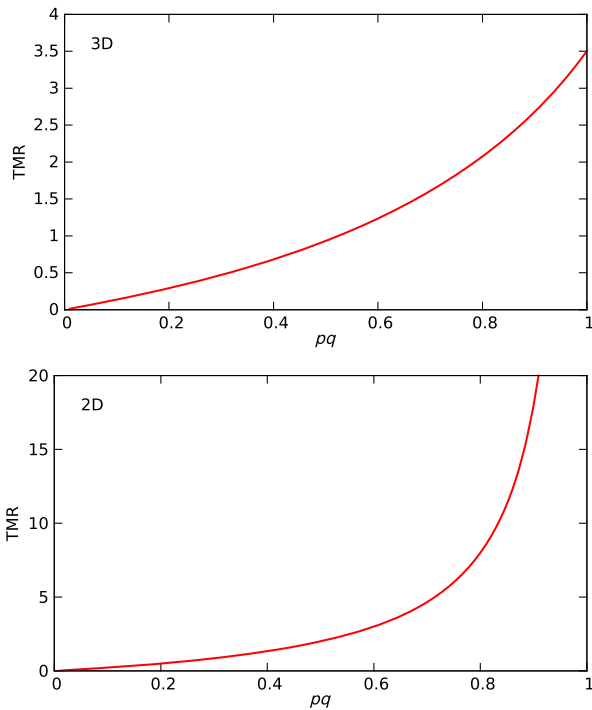

FIG. 3. Maximal TMR ratio as a function of the product of the surface state polarization p and the polarization q of the ferromagnet within the analytical approximations, Eqs. (11) and (12).

$\text{TMR}_{3D}(1, 1, \frac{\pi}{2}) \approx 3.5$ for a 3D device while it diverges in the 2D case for $pq \to 1$. The factor $\pi/2$ in the denominator of Eq. (11) as compared with Eq. (12) comes from the fact that the two-dimensional manifold of surface states on the 3D devices possesses in-plane spin polarizations of all directions, as shown in the Appendix. Even for surface states with $p = 1$ a finite amount of electrons can thus tunnel into surface states with a velocity component into the opposite direction, reducing the TMR ratio. In the 2D devices such a situation can be avoided.

For the numerical TMR ratios we calculate the eigenstates and eigenenergies of the TI by an exact diagonalization of the Fourier-transformed Hamiltonian on a lattice of size $50 \times 400 \times 400$ for setups A and B, $100 \times 400 \times 400$ for C–F, and 200×800 for G and H, where the first number is always for the direction perpendicular to the surface plane. Because of the periodic boundary conditions within the surface plane this can be done separately for all discrete in-plane momenta $\tilde{\mathbf{k}}$. To obtain the sign of the group-velocity component v_x, we compare the eigenenergies with those we get after a small variation of k_x. Assuming the FM to be large, the spatial dependence of the FM states perpendicular to the surface is given by $\sin z k_z$, where z is the lattice position and the perpendicular momentum k_z is a continuous function of the in-plane momentum $\tilde{\mathbf{k}}$ and the TI eigenenergies, satisfying energy and in-plane momentum conservation (see the Appendix). To obtain $G_{\max}(U)$ the direction of the magnetization of the ferromagnet is chosen such that the differential conductance is maximized. This maximum occurs when the magnetization direction fits the expectation value of the spin operators $\Sigma_i = \mathbb{1}_{2\times2} \otimes \sigma_i$ [38] of those TI surface states that propagate towards a metallic electrode. The TMR ratio is then calculated using Eq. (10), where the maximal and minimal differential conductances are calculated by summing only over those states with positive or negative group-velocity component v_x in Eq. (9), i.e., by looking at opposite metallic electrodes.

In Fig. 4 the results of these calculations at room temperature are shown (solid lines) in comparison with the corresponding expectation from the analytical approximation (horizontal dashed lines with the same color). The FM is chosen to be ideal for these calculations, i.e., fully polarized ($q = 1$). To make an appropriate comparison of our numerical results with the analytical approximation, we determine the polarization p of the TI surface states from the numerical calculation in the following way: we determine p from the absolute value of the spin-expectation value for a surface state having a momentum in the direction of the metallic electrode close to the Dirac point. As the magnetization of the ferromagnet is aligned to the spin of this state, the analytical formula gives the best approximation for this value of p, because the main contribution to the differential conductance comes from electrons with similar spin direction. Note that the value of
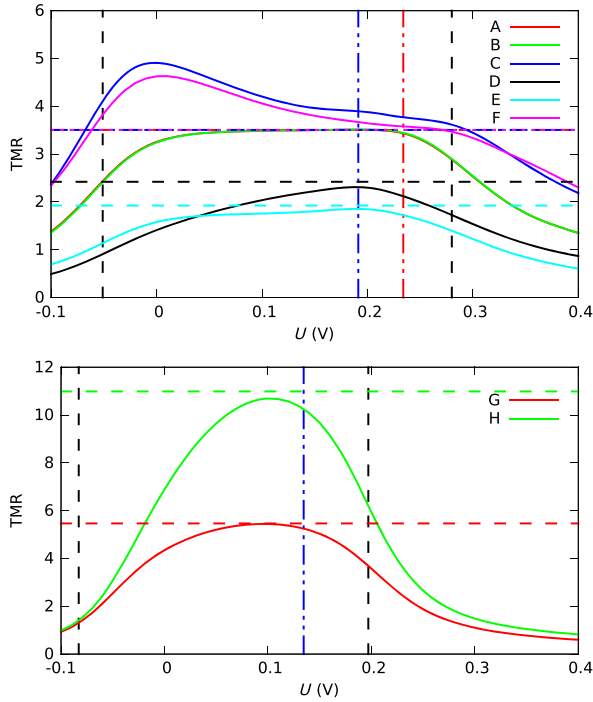
FIG. 4. TMR ratio based on numerical calculations for the different setups A–G in Fig. 2. The horizontal dashed lines represent the analytical approximation for the spin polarization p of the surface states close to the Dirac point. The energy position of the Dirac point is shown by the vertical red dash-dotted line for the [001] surface (234 meV) and the vertical blue dash-dotted line for the [100] and [$\bar{1}$20] surfaces (191 meV in the 3D case and 135 meV in the 2D case). The vertical black dashed lines denote the positions of the gap edges.

FIG. 5. Spin-expectation values of the lower Dirac cone on the side surface in the [$\bar{1}$20] direction. The declaration of the momentum components corresponds to setup D. In the upper figure the in-plane spin is shown by the arrows while the out-of-plane spin component is indicated by the color. The lines are constant energy contours. The lower figure shows the absolute value of the spin-expectation value.

p depends on the crystallographic orientation of the surface leading to different values for the different setups.

Since the surface states only exist inside the bulk gap and the bulk states are unpolarized, the TMR ratio drops towards the edges of the gap (shown by the vertical black lines). This influence of the bulk states increases with increasing temperature and may reduce the maximal TMR ratio in systems with small gaps. Taking a closer look at the different setups, setups A and B show nearly no difference and are in very good agreement with the analytical approximation $\text{TMR}_{3D} \approx 3.5$ for $p = 1$. There is only a tiny deviation for larger $\tilde{k}$, where the numerical TMR ratio decreases due to a small, albeit increasing, out-of-plane polarization of the surface states caused by hexagonal warping.

Because of the anisotropy of the [100] and [$\bar{1}$20] surfaces, the analytical approximation gives only a rough estimate for the TMR ratio of setups C–F. The anisotropy changes the shape of the Dirac cone and with it the spin orientation from circular to a more elliptical form (see Fig. 5). This anisotropy creates an imbalance in the tunneling probabilities of electrons with different spin orientations. For setups C and F the TMR ratio at the Dirac point is slightly larger than the estimated 3.5 and rises
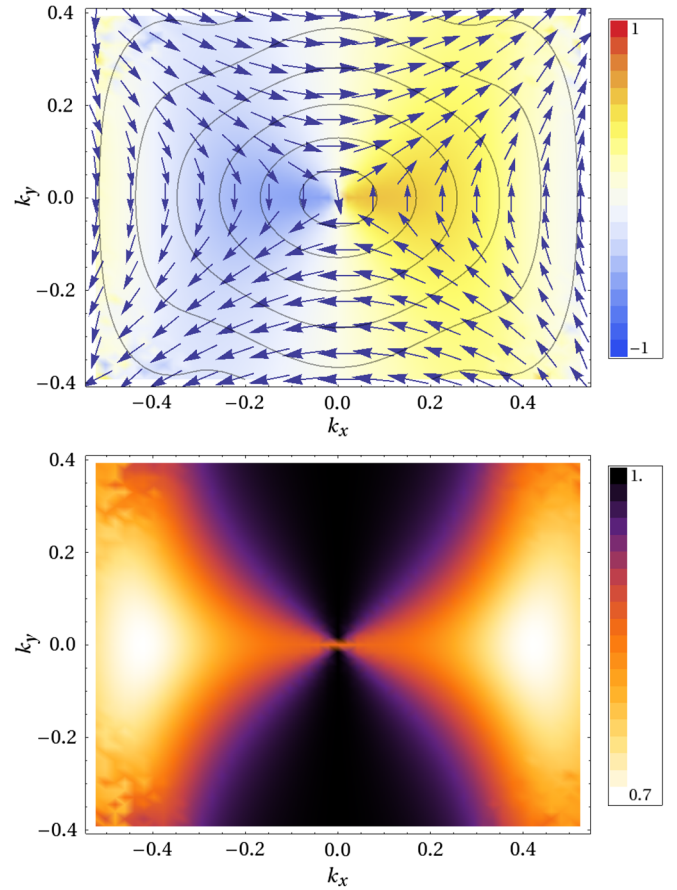
up to approximately 4.9 for setup C and approximately 4.6 for setup F near the lower edge of the bulk gap. As the TMR ratio increases away from the Dirac point, it is limited by the size of the bulk gap and the position of the Dirac point inside the gap. The fact that setup C reaches a larger value than setup F indicates that for equally polarized surfaces it is beneficial to choose the surface parallel to a crystal axis.

In contrast to setups C and F, the anisotropy reduces the TMR ratio for setups D and E, which is already smaller because the surface states have a reduced spin polarization of $p \approx 0.86$ and $p \approx 0.77$ near the Dirac point, respectively. The TMR ratio is further reduced by a change in the polarization orientation and strength as a function of energy away from the Dirac point.

In the case of a 2D device (setups G and H), the TMR ratio reaches much larger values than in the 3D case, as there are basically only two spin orientations flipping at $\tilde{k} = 0$. Near the Dirac point, the TMR ratio now falls somewhat below the analytical approximation and
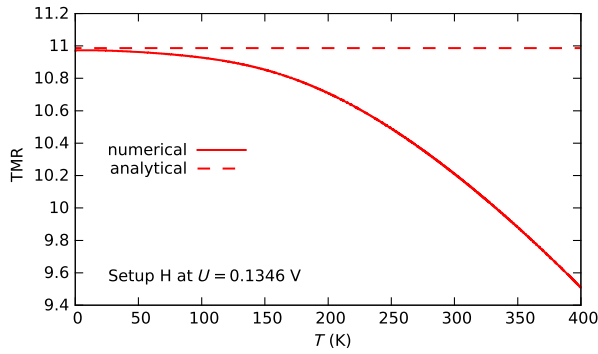
FIG. 6. Temperature dependence of the TMR ratio for the 2D setup H at the Dirac point (solid line). The dashed line shows the TMR ratio within the analytical approximation, which is reached by the numerical results at low temperature.

decreases rapidly towards the edges of the gap. On one hand this decrease is due to the higher sensitivity of the larger TMR ratios resulting in a more important influence of the bulk states. On the other hand, similar as for setups D and E, there is a change in the orientation and strength of the spin polarization as a function of energy, further reducing the TMR ratio away from the Dirac point. Still we get a maximal TMR ratio of approximately 5.4 for setup G ($p \approx 0.73$) and approximately 10.7 for setup H ($p \approx 0.85$) at room temperature.

In Fig. 6 we show the temperature dependence of the TMR ratio for setup H and bias voltage chosen at the Dirac point. Here, it is seen that the value of the analytical approximation is reached at low temperatures. This result demonstrates that the finite-temperature occupation of the bulk states somewhat mitigates the TMR ratio already at room temperature in the 2D devices.

The 2D devices (setups G and H) reach much larger TMR values than the 3D ones. However, they are technically more challenging to realize as the tunneling barrier has to be attached to the edge states of a thin TI film. In Fig. 7 we propose an alternative 3D device, which is easier to realize than the 2D devices, but which approaches the same large TMR values. In this device one of the two metallic electrodes is U shaped and is supposed to capture most electrons that do not propagate in a positive x direction from the ferromagnetic to the other, smaller metallic electrode. As a result, the electrons that reach the smaller metallic electrode preferentially possess only a single spin orientation. Thus, the transport between the ferromagnetic and the smaller metallic electrode approaches a one-dimensional transport, similarly as in the edge states of the 2D devices. We apply our analytical approximation to this geometry (for more details see the Appendix), corresponding to a [001] surface, i.e., the crystallographic orientation of setup A. In Fig. 8 the TMR ratio of this U-shaped device is shown as a function of the ratio d/h, where d is the distance between the ferromagnetic and the smaller metallic electrode, and h is the height
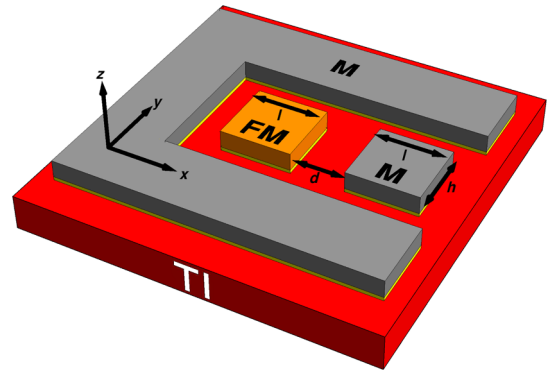

FIG. 7. Alternative device on the surface of a 3D TI which allows us to approach the large TMR ratios of a 2D device. The U-shaped metallic electrode captures nearly all electrons moving in other directions than the positive x direction. The ferromagnetic electrode and the smaller metallic one possess length l and height h. The distance between them is d.

of the electrodes as shown in Fig. 7. In this calculation we assumed that the ferromagnetic and the smaller metallic electrode are square shaped, i.e., $l = h$. For illustration, we assumed that the product pq of the polarizations of the ferromagnet and the topological insulator is 0.8. As Fig. 8 shows, the U-shaped 3D device yields much larger TMR values than the 3D devices. For $d/h \gg 1$ the TMR ratio of the U-shaped device approaches the TMR ratio of the 2D device, which is clear as with increasing distance d the angular range of topological surface states that can reach the metallic electrode is gradually reduced and focused.

The calculations we report here are done with parameters appropriate for undoped Bi_2Se_3, as pointed out above. However, in practice these materials often appear to be intrinsically doped [6,7], which shifts the Fermi level with respect to the surface Dirac cone. For Bi_2Se_3 a Fermi-level shift of 200 meV is reported [6]. We want to point out that the functionality of the devices proposed here is not affected by such intrinsic doping. The Fermi-level shift will shift the energies E_n of the topological surface states
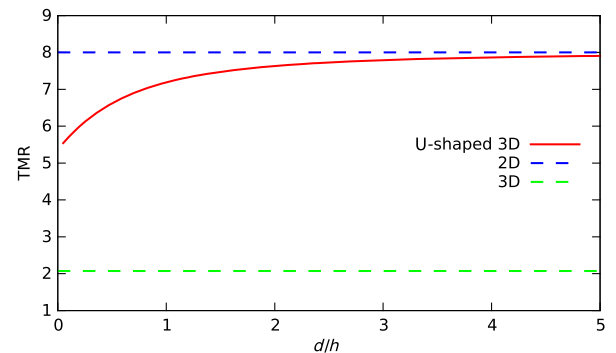

FIG. 8. TMR ratio near the Dirac point for the device shown in Fig. 7 as a function of d/h for $l = h$ and $pq = 0.8$. A higher ratio l/h further increases the TMR ratio. The dashed lines show the results of the 2D and 3D devices discussed above.

with respect to the ones of the ferromagnet. This energy shift can be fully compensated for by a shift of the bias voltage U in Eq. (9) leading to a bias voltage shift of our results in Fig. 4. Thus, the high TMR ratios will be robust against intrinsic doping, but just appear at a shifted bias voltage.

While our calculations find a full spin polarization for the [001] surface, consistent with recent spin- and angle-resolved photoemission spectroscopy (SARPES) measurements of Pan *et al.* [39], the spin polarization in Bi_2Se_3 is still controversial. The reported spin polarization ranges from 50%–65% in first-principle calculations [40–42] to 75%–80% or more in SARPES measurements [12,43]. If we consider these values, according to Fig. 3 the TMR ratio could be reduced to approximately 0.9–2 in the 3D devices and approximately 2–8 in the 2D devices, which is still large, though.

As our analytical formulas for the TMR ratio Eqs. (11) and (12) depend only on the spin polarization and not on the exact parametrization, they are universally valid for all materials in the limit of an isotropic surface. In contrast, the TMR ratio for an anisotropic surface strongly depends on the model parameters and the deviation from the isotropic solution may therefore be different for other materials.

In the present work, we focus on Bi_2Se_3, which has been studied well in the past. Considering other materials, $TlBiSe_2$ could also be a good candidate for TMR devices as discussed here, because it has an in-plane spin polarization of approximately 80%, a negligible out-of-plane polarization, and a large bulk gap of approximately 0.35 eV [44–46]. The high spin polarization of 80%–90% of Sb_2Te_3 promises a high TMR ratio, too. However, at room temperature it will probably be reduced because of the small bulk gap of only approximately 0.2 eV [47]. Bi_2Te_3 and $Pb(Bi, Sb)_2Te_4$ seem to be less attractive since they have in-plane spin polarizations of only 45%–60% [40,45,48,49] and 50% [50] and small bulk gaps of only about 0.08–0.165 eV [5,40] and 0.2–0.23 eV [8,51], respectively. They also possess a significant out-of-plane polarization due to the hexagonal deformation of the Fermi surface [40,45,48,50].

An attractive feature of the devices proposed here is the topological protection of the spin-locked surface states, which makes them particularly robust against perturbations. In usual TMR junctions defects close to the interface can substantially suppress the TMR ratio, in particular at high temperature [52,53]. For the present devices we have to distinguish nonmagnetic and magnetic scattering mechanisms. Nonmagnetic scattering processes, such as disorder or faceting of the barrier, which scatter the momentum of an electron during the transfer from the ferromagnet to the topological insulator, but keep its spin conserved, are only weakly affecting our TMR results, because the TMR ratio is predominantly dictated by the helical spin structure of the surface states, which is topologically protected. As long as

the spin is conserved, momentum scattering does not change our results, as the total current already consists of contributions from all momentum directions. Magnetic scattering mechanisms, on the other hand, do reduce the TMR ratio. This is obvious, as a spin-flip process during tunneling will change the direction of flow in the topological surface state. Such processes could be modeled by a reduced apparent polarization q of the ferromagnet seen by the topological insulator. An experimental realization of our devices should thus take care to avoid magnetic scattering in the barrier. These are the same quality requirements as for conventional TMR devices based on magnetic tunnel junctions and have been successfully dealt with in the past, however.

The distance chosen between the electrodes should be sufficiently small such that electrons traveling from the ferromagnetic electrode to one metallic electrode are not backscattered to the opposite metallic electrode in between. As the surface states are topologically protected by time-reversal symmetry, such backscattering is strongly suppressed and can only occur when time-reversal symmetry-breaking scattering impurities or imperfections exist in the topological insulator. Thus, the distance between the electrodes should be smaller than the spin-flip mean free path of the surface states. Values of the order of 2 μm are reported [54,55]. It has been demonstrated in the past that magnetic tunnel junctions can be structured down to a 50 nanometer scale [56].

In conventional semiconductor Rashba devices TMR ratios of up to 50% are reached at room temperature [57,58]. For TMR devices based on magnetic tunnel junctions with two ferromagnetic electrodes reported TMR ratios range between 180% and 600% [52,53,59–62]. The TMR values calculated here are comparable to or larger than these values.

IV. SUMMARY AND CONCLUSIONS

In the present work we propose specific setups to build TMR devices exploiting the topological-insulator material Bi_2Se_3. Using a realistic tight-binding model we calculate the achievable TMR ratios as a function of bias voltage and temperature. If the bias voltage is chosen properly, we find that room temperature TMR ratios of 490% can be achieved in the 3D devices and 1070% in the 2D devices. We suggest a U-shaped 3D device, which is experimentally easier to realize than the 2D devices, but reaches correspondingly high TMR values. We derive simple analytical formulas for the devices, which provide a quick approximate figure of merit once the surface-state polarization of a given topological insulator is known. For the 3D devices we show that on an anisotropic surface the TMR ratio may become larger than the one estimated from the analytical formula. In contrast to conventional TMR devices the devices proposed here do not need a second ferromagnetic layer, as an intrinsic magnetic reference direction is already provided

by the topological insulator. In addition, the present devices provide a means to experimentally probe the surface-state polarization of a given topological insulator.

APPENDIX: ANALYTICAL TMR RATIO

In this Appendix we derive an analytical approximation for the TMR ratio. We base this derivation on an analytical approximation of the surface states only and neglect the effects of bulk states. Considering the large bulk gap of Bi_2Se_3, this should be a good approximation even at room temperature.

To find an analytical approximation of the surface states for a surface at $z = 0$, we expand Hamiltonian equation (1) up to second order in k_z. As a starting point, we first neglect all k_x- and k_y-dependent terms by setting $k_x = k_y = 0$. If we assume the TI to be half infinite with its boundary at $z = 0$, we have to replace k_z with the momentum operator $-i\partial_z$ and search for nontrivial solutions that vanish both at $z = 0$ and for $z \to \infty$. There exist two degenerate eigen-states with energy $E = -\frac{C_1 M_0}{M_1}$ satisfying both conditions:

$$\psi_1(z) = \frac{1}{N} \begin{pmatrix} \sqrt{\frac{M_1 - C_1}{2M_1}} \\ 0 \\ \sqrt{\frac{M_1 + C_1}{2M_1}} \\ 0 \end{pmatrix} (e^{-\alpha_1 z} - e^{-\alpha_2 z}), \quad (A1)$$

$$\psi_2(z) = \frac{1}{N} \begin{pmatrix} 0 \\ \sqrt{\frac{M_1 - C_1}{2M_1}} \\ 0 \\ \sqrt{\frac{M_1 + C_1}{2M_1}} \end{pmatrix} (e^{-\alpha_1 z} - e^{-\alpha_2 z}), \quad (A2)$$

with $\alpha_1 \neq \alpha_2$, $\mathrm{Re}\,\alpha_{1/2} > 0$ and some normalization constant N for the z-dependent part. Next, we treat the neglected k_x- and k_y-dependent terms as a perturbation using degenerate perturbation theory and get the new surface states

$$\psi_\pm(k_x, k_y, z) = u_1 \psi_1 + u_2 \psi_2, \quad (A3)$$

with

$$u_1(k_x, k_y) = -\frac{(m_1 - im_2)\mathrm{sgn}(\mathcal{R}_1 \mp \sqrt{m_1^2 + m_2^2 + \mathcal{R}_1^2})}{\sqrt{m_1^2 + m_2^2 + (\mathcal{R}_1 \mp \sqrt{m_1^2 + m_2^2 + \mathcal{R}_1^2})^2}}, \quad (A4)$$

$$u_2(k_x, k_y) = \frac{\sqrt{(\mathcal{R}_1 \mp \sqrt{m_1^2 + m_2^2 + \mathcal{R}_1^2})^2}}{\sqrt{m_1^2 + m_2^2 + (\mathcal{R}_1 \mp \sqrt{m_1^2 + m_2^2 + \mathcal{R}_1^2})^2}}. \quad (A5)$$

The perturbed eigenenergies are

$$E_\pm = -\frac{C_1 M_0}{M_1} + \epsilon_0' - \frac{C_1}{M_1} m_4'$$
$$\pm \sqrt{(m_1^2 + m_2^2 + \mathcal{R}_1^2)\left(1 - \frac{C_1^2}{M_1^2}\right)}. \quad (A6)$$

Here, $\epsilon_0' = \frac{4}{3} C_2 (3 - 2\cos\frac{1}{2}k_x \cos\frac{\sqrt{3}}{2}k_y - \cos k_x)$ and $m_4' = \frac{4}{3} M_2 (3 - 2\cos\frac{1}{2}k_x \cos\frac{\sqrt{3}}{2}k_y - \cos k_x)$ and $\pm$ is for the upper and lower Dirac cone, respectively. If we expand u_1, u_2, and $E_\pm$ up to second order in k_x and k_y, the solutions become isotropic in the k_x-k_y plane and we can write $\psi_\pm$ solely as a function of z and the in-plane polar angle φ. The energies $E_\pm$ then become

$$E_\pm = -\frac{C_1 M_0}{M_1} + \left(C_2 - \frac{C_1}{M_1}M_2\right)k^2 \pm A_0\sqrt{1 - \frac{C_1^2}{M_1^2}}k, \quad (A7)$$

and thus only depend on the magnitude $k = \sqrt{k_x^2 + k_y^2}$. This expression agrees with the one derived previously in Ref. [27].

Calculation of the expectation values of the spin oper-ators $\Sigma_i = \mathbb{1}_{2\times 2} \otimes \sigma_i$ [38] shows that the spin of these surface states is always perpendicular to the in-plane momentum and lies within the surface plane. As the direction of the spin is the same for both orbitals, this model yields surface states which are fully polarized, at least at the [001] surface. Here, we allow for a finite spin polarization $0 \leq p \leq 1$ and thus rewrite the surface-state wave functions as a function of polarization p

$$\psi_\pm(p, \varphi) = \frac{1}{2} \begin{pmatrix} \pm\sqrt{1 + p}\,e^{-i[\varphi - (\pi/2)]} \\ \sqrt{1 + p} \\ \mp \sqrt{1 - p}\,e^{-i[\varphi - (\pi/2)]} \\ \sqrt{1 - p} \end{pmatrix}. \quad (A8)$$

As all constant prefactors cancel in the TMR ratio, we neglect these as well as the spatial dependence, because in the calculation of the tunneling current only the lattice position next to the barrier plays a role. The spatial dependence of the FM states perpendicular to the surface is a superposition of an incoming plane wave e^{izk_z} with the reflected one e^{-izk_z} having a node inside the barrier (at $z = 0$) and is thus given by $\sin zk_z$. Note that this is an exact solution of the tight-binding model for a thick FM with zero transmission probability through the barrier. Here, the momentum k_z is a continuous function of the in-plane momentum k and the TI eigenenergies $E_\pm$, satisfying energy and in-plane momentum conservation:

$$k_z(k) = \arccos\frac{C_F(2 + k^2) \pm W - E_\pm}{2C_F}. \quad (A9)$$

Since the spin of the surface states lies within the surface plane it is sufficient to write the states of the FM as a function of the in-plane polar angle φ_F

$$\psi_F(k,\varphi_F) = \frac{1}{2}\sin k_z(k)(e^{-i\varphi_F}, 1, e^{-i\varphi_F}, 1). \quad (A10)$$

The transfer matrix elements

$$|\langle\psi_F|H_T|\psi_\pm\rangle|^2 = C_B^2\sin^2 k_z(k)[1 \mp p\sin(\varphi_F - \varphi)] \quad (A11)$$

can then be inserted into Eq. (9).

In the calculation of the differential conductance the geometry of the device can be accounted for by an additional angular-dependent factor $f(\varphi)$. This factor describes the probability that an electron starting its propagation in the TI at an angle φ below the FM electrode ends up at the metallic electrode at $x > 0$ averaged over the spatial extend of the two electrodes. Under the assumption that $f(\varphi) = f(-\varphi)$, which holds for a device which is mirror symmetric with respect to the x-z plane and valid for all devices considered in this work, the φ integral can be separated from the rest of the differential conductance

$$G(T,U,\varphi_F) = \frac{\text{const}}{T}\int_0^{k_0} dk\, k\int_{-\pi}^{\pi} d\varphi\left(f(\varphi)\frac{|\langle\psi_F|H_T|\psi_+\rangle|^2}{\cosh^2(\frac{E_+ - eU}{2k_BT})}\right.$$
$$\left. + f(\varphi - \pi)\frac{|\langle\psi_F|H_T|\psi_-\rangle|^2}{\cosh^2(\frac{E_- - eU}{2k_BT})}\right)$$
$$= \int_{-\pi}^{\pi} d\varphi\, f(\varphi)(1 - p\sin\varphi_F\cos\varphi)G'(T,U),$$

$$(A12)$$

with the function

$$G'(T,U) = \frac{\text{const}}{T}\int_0^{k_0} dk\, k\left(\frac{\sin^2 k_z(k)}{\cosh^2(\frac{E_+ - eU}{2k_BT})} + \frac{\sin^2 k_z(k)}{\cosh^2(\frac{E_- - eU}{2k_BT})}\right),$$

$$(A13)$$

which is independent of φ_F.

Up to this point we considered an ideal FM, i.e., fully polarized. To account for a finite polarization $q = n_+ - n_-$ of the FM we have to replace $G(T,U,\varphi_F)$ by

$$G''(T,U,\varphi_F) = n_+G(T,U,\varphi_F) + n_-G(T,U,-\varphi_F)$$
$$= \int_{-\pi}^{\pi} d\varphi\, f(\varphi)(1 - pq\sin\varphi_F\cos\varphi)G'(T,U).$$

$$(A14)$$

Here, $0 \le n_\pm \le 1$ with $n_+ + n_- = 1$ is the relative density of states of electrons in the FM with spin projection parallel (+) or antiparallel (−) to the polarization angle φ_F. Defining

$$\gamma = \frac{\int_{-\pi}^{\pi} d\varphi\, f(\varphi)}{\int_{-\pi}^{\pi} d\varphi\, f(\varphi)\cos\varphi}, \quad (A15)$$

the TMR ratio

$$\text{TMR}(p,q,\varphi_F) = \frac{1 + \sin\varphi_F}{\frac{\gamma}{pq} - \sin\varphi_F} \quad (A16)$$

depends only on p, q, and φ_F. In particular, it does not depend on temperature, because the temperature dependence of the differential conductance $G'(T,U)$ is the same in all directions due to the in-plane rotational symmetry of the surface states and thus drops out in the TMR ratio. This temperature independence is lost, of course, if the contribution of the bulk states is included. The geometry of the device appears only via the single parameter γ. This parameter can now be calculated for different geometries of the devices. For setups A–H we assume that all electrons initially moving in the positive x direction end up at the electrode at $x > 0$ and all others at the counterelectrode. For the 3D devices A–F the function $f(\varphi)$ is then simply given by

$$f(\varphi) = \begin{cases} 1 & \text{if } \varphi \in [-\frac{\pi}{2}, \frac{\pi}{2}] \\ 0 & \text{else,} \end{cases} \quad (A17)$$

which yields $\gamma = \frac{\pi}{2}$. For the 2D devices G and H we have

$$f(\varphi) = \delta(\varphi), \quad (A18)$$

giving $\gamma = 1$. For the device shown in Fig. 7 we can derive $f(\varphi)$ from the sketch shown in Fig. 9. Considering an electron starting from the FM at an angle φ on a vertical line with distance x from a vertical line in the metallic electrode (M), it can reach that line only if it comes from the fraction $h' = h - x\tan\varphi$, i.e., the mean probability to reach the line is $\frac{h'}{h} = (1 - \frac{x}{h}\tan|\varphi|)$ if $|\varphi| \le \varphi_m = \arctan\frac{h}{x}$ and otherwise zero. Averaging over the length l of the FM and the metallic electrode results in
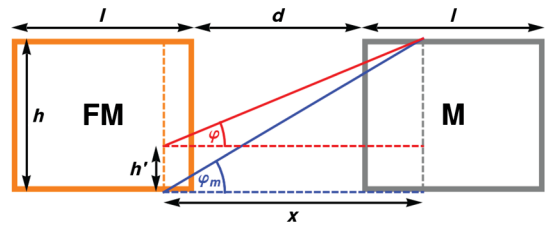

FIG. 9. Sketch of the electrodes in the device from Fig. 7, illustrating the calculation of the angular probability distribution $f(\varphi)$.
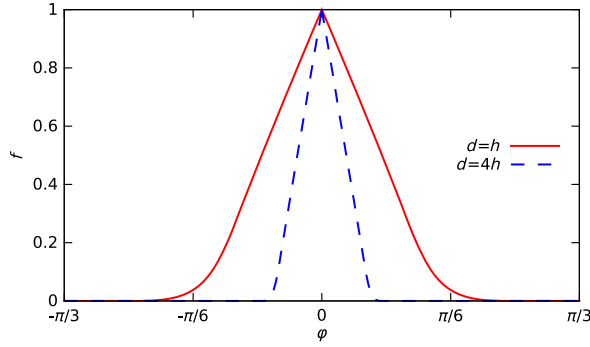
FIG. 10.   The function $f(\varphi)$ Eq. (A19) for $l = h$ and $d = h$ (red solid line) as well as $d = 4h$ (blue dashed line).

$$f(\varphi) = \int_{d}^{d+2l} dx \, \frac{l - |x - d - l|}{l^2}$$
$$\times \left(1 - \frac{x}{h}\tan|\varphi|\right)\Theta\left(\arctan\frac{h}{x} - |\varphi|\right), \quad \text{(A19)}$$

where Θ is the Heaviside step function. γ can then be calculated numerically for specific values of d, l, and h. In Fig. 10 this function $f(\varphi)$ is shown for $l = h$ and $d = h$ as well as $d = 4h$, showing that for the larger value of d the angular dependence becomes more strongly focused near $\varphi = 0$.

[1] B. A. Bernevig, T. L. Hughes, and S.-C. Zhang, Quantum spin Hall effect and topological phase transition in HgTe quantum wells, Science **314**, 1757 (2006).

[2] L. Fu, C. L. Kane, and E. J. Mele, Topological insulators in three dimensions, Phys. Rev. Lett. **98**, 106803 (2007).

[3] M. König, S. Wiedmann, C. Brüne, A. Roth, H. Buhmann, L. W. Molenkamp, X.-L. Qi, and S.-C. Zhang, Quantum spin Hall insulator state in HgTe quantum wells, Science **318**, 766 (2007).

[4] D. Hsieh, D. Qian, L. Wray, Y. Xia, Y. Hor, R. J. Cava, and M. Z. Hasan, A topological Dirac insulator in a quantum spin Hall phase, Nature (London) **452**, 970 (2008).

[5] Y. L. Chen, J. G. Analytis, J.-H. Chu, Z. K. Liu, S.-K. Mo, X. L. Qi, H. J. Zhang, D. H. Lu, X. Dai, Z. Fang, S. C. Zhang, I. R. Fisher, Z. Hussain, and Z.-X. Shen, Experimental realization of a three-dimensional topological insulator, Bi$_2$Te$_3$, Science **325**, 178 (2009).

[6] Y. Xia, D. Qian, D. Hsieh, L. Wray, A. Pal, H. Lin, A. Bansil, D. Grauer, Y. S. Hor, R. J. Cava, and M. Z. Hasan, Observation of a large-gap topological-insulator class with a single Dirac cone on the surface, Nat. Phys. **5**, 398 (2009).

[7] D. Hsieh, Y. Xia, D. Qian, L. Wray, F. Meier, J. H. Dil, J. Osterwalder, L. Patthey, A. V. Fedorov, H. Lin, A. Bansil, D. Grauer, Y. S. Hor, R. J. Cava, and M. Z. Hasan, Observation of time-reversal-protected single-Dirac-cone topological-insulator states in Bi$_2$Te$_3$ and Sb$_2$Te$_3$, Phys. Rev. Lett. **103**, 146401 (2009).

[8] K. Kuroda, H. Miyahara, M. Ye, S. V. Eremeev, Yu. M. Koroteev, E. E. Krasovskii, E. V. Chulkov, S. Hiramoto,

C. Moriyoshi, Y. Kuroiwa, K. Miyamoto, T. Okuda, M. Arita, K. Shimada, H. Namatame, M. Taniguchi, Y. Ueda, and A. Kimura, Experimental verification of PbBi$_2$Te$_4$ as a 3D topological insulator, Phys. Rev. Lett. **108**, 206803 (2012).

[9] Y. Ando, Topological insulator materials, J. Phys. Soc. Jpn. **82**, 102001 (2013).

[10] D. Hsieh, Y. Xia, D. Qian, L. Wray, J. H. Dil, F. Meier, J. Osterwalder, L. Patthey, J. G. Checkelsky, N. P. Ong, A. V. Fedorov, H. Lin, A. Bansil, D. Grauer, Y. S. Hor, R. J. Cava, and M. Z. Hasan, A tunable topological insulator in the spin helical Dirac transport regime, Nature (London) **460**, 1101 (2009).

[11] C. Brüne, A. Roth, H. Buhmann, E. M. Hankiewicz, L. W. Molenkamp, J. Maciejko, X.-L. Qi, and S.-C. Zhang, Spin polarization of the quantum spin Hall edge states, Nat. Phys. **8**, 485 (2012).

[12] Z.-H. Pan, E. Vescovo, A. V. Fedorov, D. Gardner, Y. S. Lee, S. Chu, G. D. Gu, and T. Valla, Electronic structure of the topological insulator Bi$_2$Se$_3$ using angle-resolved photoemission spectroscopy: Evidence for a nearly full surface spin polarization, Phys. Rev. Lett. **106**, 257004 (2011).

[13] Y. Tanaka, T. Yokoyama, and N. Nagaosa, Manipulation of the majorana fermion, Andreev reflection, and Josephson current on topological insulators, Phys. Rev. Lett. **103**, 107002 (2009).

[14] S. Mondal, D. Sen, K. Sengupta, and R. Shankar, Tuning the conductance of Dirac fermions on the surface of a topological insulator, Phys. Rev. Lett. **104**, 046403 (2010).

[15] J. Linder, Y. Tanaka, T. Yokoyama, A. Sudbo, and N. Nagaosa, Unconventional superconductivity on a topological insulator, Phys. Rev. Lett. **104**, 067001 (2010).

[16] I. Garate and M. Franz, Inverse spin-galvanic effect in the interface between a topological insulator and a ferromagnet, Phys. Rev. Lett. **104**, 146802 (2010).

[17] T. Yokoyama, Y. Tanaka, and N. Nagaosa, Anomalous magnetoresistance of a two-dimensional ferromagnet/ferromagnet junction on the surface of a topological insulator, Phys. Rev. B **81**, 121401 (2010).

[18] A. M. Black-Schaffer and J. Linder, Majorana fermions in spin-orbit-coupled ferromagnetic Josephson junctions, Phys. Rev. B **84**, 180509(R) (2011).

[19] V. Krueckl and K. Richter, Switching spin and charge between edge states in topological insulator constrictions, Phys. Rev. Lett. **107**, 086803 (2011).

[20] B. D. Kong, Y. G. Semenov, C. M. Krowne, and K. W. Kim, Unusual magnetoresistance in a topological insulator with a single ferromagnetic barrier, Appl. Phys. Lett. **98**, 243112 (2011).

[21] M. Salehi, M. Alidoust, Y.Rahnavard, and G.Rashedi, In-plane magnetoresistance on the surface of topological insulator, Physica (Amsterdam) **43E** , 966 (2011).

[22] R. Vali and M. Vali, Tunneling conductance and magnetoresistance in topological insulator Fi/I/Fi/d-wave superconductor junctions, J. Appl. Phys. **112**, 103919 (2012).

[23] T. Paananen, H. Gerber, M. Götte, and T. Dahm, Appearance of flat surface bands in three-dimensional topological insulators in a ferromagnetic exchange field, New J. Phys. **16**, 033019 (2014).

[24] K. Taguchi, T. Yokoyama, and Y. Tanaka, Giant magneto-resistance in the junction of two ferromagnets on the surface of diffusive topological insulators, Phys. Rev. B **89,** 085407 (2014).

[25] R. Li, J. Wang, X.-L. Qi, and S.-C. Zhang, Dynamical axion field in topological magnetic insulators, Nat. Phys. **6,** 284 (2010).

[26] H. Zhang, C.-X. Liu, X.-L. Qi, X. Dai, Z. Fang, and S.-C. Zhang, Topological insulators in Bi_2Se_3, Bi_2Te_3 and Sb_2Te_3 with a single Dirac cone on the surface, Nat. Phys. **5,** 438 (2009).

[27] W.-Y. Shan, H.-Z. Lu, and S.-Q. Shen, Effective continuous model for surface states and thin films of three-dimensional topological insulators, New J. Phys. **12,** 043048 (2010).

[28] C.-X. Liu, X.-L. Qi, H. J. Zhang, X. Dai, Z. Fang, and S.-C. Zhang, Model Hamiltonian for topological insulators, Phys. Rev. B **82,** 045122 (2010).

[29] L. Hao and T. K. Lee, Surface spectral function in the superconducting state of a topological insulator, Phys. Rev. B **83,** 134516 (2011).

[30] H. Okamoto, The Bi-Se (bismuth-selenium) system, J. Phase Equilib. **15,** 195 (1994).

[31] H. Lind, S. Lidin, and U. Häussermann, Structure and bonding properties of $(Bi_2Se_3)_m(Bi_2)_n$ stacks by first-principles density functional theory, Phys. Rev. B **72,** 184101 (2005).

[32] G. Zhang, H. Qin, J. Teng, J. Guo, Q. Guo, X. Dai, Z. Fang, and K. Wu, Quintuple-layer epitaxy of thin films of topological insulator Bi_2Se_3, Appl. Phys. Lett. **95,** 053114 (2009).

[33] L. Fu, Hexagonal warping effects in the surface states of the topological insulator Bi_2Te_3, Phys. Rev. Lett. **103,** 266801 (2009).

[34] Yi Zhang *et al.*, Crossover of the three-dimensional topological insulator Bi_2Se_3 to the two-dimensional limit, Nat. Phys. **6,** 584 (2010).

[35] T. Paananen and T. Dahm, Magnetically robust topological edge states and flat bands, Phys. Rev. B **87,** 195447 (2013).

[36] R. E. Prange, Tunneling from a many-particle point of view, Phys. Rev. **131,** 1083 (1963).

[37] G. D. Mahan, *Many-Particle Physics*, 2nd ed. (Plenum Press, New York, 1990).

[38] P. G. Silvestrov, P. W. Brouwer, and E. G. Mishchenko, Spin and charge structure of the surface states in topological insulators, Phys. Rev. B **86,** 075302 (2012).

[39] Z.-H. Pan, E. Vescovo, A. V. Fedorov, G. D. Gu, and T. Valla, Persistent coherence and spin polarization of topological surface states on topological insulators, Phys. Rev. B **88,** 041101(R) (2013).

[40] O. V. Yazyev, J. E. Moore, and S. G. Louie, Spin polarization and transport of surface states in the topological insulators Bi_2Se_3 and Bi_2Te_3 from first principles, Phys. Rev. Lett. **105,** 266806 (2010).

[41] X. Wang, G. Bian, T. Miller, and T.-C. Chiang, Topological spin-polarized electron layer above the surface of Ca-terminated Bi_2Se_3, Phys. Rev. B **87,** 035109 (2013).

[42] J. Sánchez-Barriga *et al.*, Photoemission of Bi_2Se_3 with circularly polarized light: Probe of spin polarization or means for spin manipulation?, Phys. Rev. X **4,** 011046 (2014).

[43] C. Jozwiak, Y. L. Chen, A. V. Fedorov, J. G. Analytis, C. R. Rotundu, A. K. Schmid, J. D. Denlinger, Y.-D. Chuang, D.-H. Lee, I. R. Fisher, R. J. Birgeneau, Z.-X. Shen, Z. Hussain, and A. Lanzara, Widespread spin polarization effects in photoemission from topological insulators, Phys. Rev. B **84,** 165113 (2011).

[44] S. Souma, M. Komatsu, M. Nomura, T. Sato, A. Takayama, T. Takahashi, K. Eto, K. Segawa, and Y. Ando, Spin polarization of gapped Dirac surface states near the topological phase transition in $TlBi(S_{1-x}Se_x)_2$, Phys. Rev. Lett. **109,** 186804 (2012).

[45] S. Souma, K. Kosaka, T. Sato, M. Komatsu, A. Takayama, T. Takahashi, M. Kriener, K. Segawa, and Y. Ando, Direct measurement of the out-of-plane spin texture in the Dirac-cone surface state of a topological insulator, Phys. Rev. Lett. **106,** 216803 (2011).

[46] T. Sato, K. Segawa, H. Guo, K. Sugawara, S. Souma, T. Takahashi, and Y. Ando, Direct evidence for the Dirac-cone topological surface states in the ternary chalcogenide $TlBiSe_2$, Phys. Rev. Lett. **105,** 136802 (2010).

[47] C. Pauly, G. Bihlmayer, M. Liebmann, M. Grob, A. Georgi, D. Subramaniam, M. R. Scholz, J. Sanchez-Barriga, A. Varykhalov, S. Blügel, O. Rader, and M. Morgenstern, Probing two topological surface bands of Sb_2Te_3 by spin-polarized photoemission spectroscopy, Phys. Rev. B **86,** 235106 (2012).

[48] A. Herdt, L. Plucinski, G. Bihlmayer, G. Mussler, S. Döring, J. Krumrain, D. Grützmacher, S. Blügel, and C. M. Schneider, Spin-polarization limit in Bi_2Te_3 Dirac cone studied by angle- and spin-resolved photoemission experiments and *ab initio* calculations, Phys. Rev. B **87,** 035127 (2013).

[49] However, a spin polarization of 75%–80% in Bi_2Te_3 has been reported in M. R. Scholz *et al.*, Reversal of the Circular Dichroism in Angle-Resolved Photoemission from Bi_2Te_3, Phys. Rev. Lett. **110,** 216801 (2013).

[50] M. Nomura, S. Souma, A. Takayama, T. Sato, T. Takahashi, K. Eto, K. Segawa, and Y. Ando, Relationship between Fermi surface warping and out-of-plane spin polarization in topological insulators: A view from spin- and angle-resolved photoemission, Phys. Rev. B **89,** 045134 (2014).

[51] S. Souma, K. Eto, M. Nomura, K. Nakayama, T. Sato, T. Takahashi, K. Segawa, and Y. Ando, Topological surface states in lead-based ternary telluride $Pb(Bi_{1-x}Sb_x)_2Te_4$, Phys. Rev. Lett. **108,** 116801 (2012).

[52] M. Yamamoto, T. Ishikawa, T. Taira, G.-F. Li, K. Matsuda, and T. Uemura, Effect of defects in Heusler alloy thin films on spin-dependent tunnelling characteristics of $Co_2MnSi/MgO/Co_2MnSi$ and $Co_2MnGe/MgO/Co_2MnGe$ magnetic tunnel junctions, J. Phys. Condens. Matter **22,** 164212 (2010).

[53] V. Drewello, D. Ebke, M. Schäfers, Z. Kugler, G. Reiss, and A. Thomas, Magnon excitation and temperature dependent transport properties in magnetic tunnel junctions with Heusler compound electrodes, J. Appl. Phys. **111,** 07C701 (2012).

[54] M. König, H. Buhmann, L. W. Molenkamp, T. Hughes, C.-X. Liu, X.-L. Qi, and S.-C. Zhang, The quantum spin Hall effect: Theory and experiment, J. Phys. Soc. Jpn. **77,** 031007 (2008).

[55] M. König, M. Baenninger, A. G. F. Garcia, N. Harjee, B. L. Pruitt, C. Ames, P. Leubner, C. Brüne, H. Buhmann, L. W. Molenkamp, and D. Goldhaber-Gordon, Spatially resolved study of backscattering in the quantum spin Hall state, Phys. Rev. X **3**, 021003 (2013).

[56] H. Kubota, Y. Ando, T. Miyazaki, G. Reiss, H. Brückl, W. Schepper, J. Wecker, and G. Gieres, Size dependence of switching field of magnetic tunnel junctions down to 50 nm scale, J. Appl. Phys. **94**, 2028 (2003).

[57] P. Wójcik, J. Adamowski, B. J. Spisak, and M. Wooszyn, J. Appl. Phys. **115**, 104310 (2014).

[58] K. Yoh, Z. Cui, K. Konishi, M. Ohno, K. Blekker, W. Prost, F.-J. Tegude, and J.-C. Harmand, An InAs nanowire spin transistor with subthreshold slope of 20 mV/dec, in *Proceedings of the IEEE 70th Annual Device Research Conference* (IEEE, University Park, Texas, 2012), p. 79 [http://ieeexplore .ieee.org/xpl/articleDetails.jsp?arnumber=6256935].

[59] S. S. Parkin, C. Kaiser, A. Panchula, P. M. Rice, B. Hughes, M. Samant, and S.-H. Yang, Giant tunnelling magnetoresistance at room temperature with MgO (100) tunnel barriers, Nat. Mater. **3**, 862 (2004).

[60] S. Yuasa, T. Nagahama, A. Fukushima, Y. Suzuki, and K. Ando, Giant room-temperature magnetoresistance in single-crystal Fe/MgO/Fe magnetic tunnel junctions, Nat. Mater. **3**, 868 (2004).

[61] S. Ikeda, J. Hayakawa, Y. Ashizawa, Y. M. Lee, K. Miura, H. Hasegawa, M. Tsunoda, F. Matsukura, and H. Ohno, Tunnel magnetoresistance of 604% at 300 K by suppression of Ta diffusion in CoFeB/MgO/CoFeB pseudo-spin-valves annealed at high temperature, Appl. Phys. Lett. **93**, 082508 (2008).

[62] H.-X. Liu, Y. Honda, T. Taira, K. Matsuda, M. Arita, T. Uemura, and M. Yamamoto, Giant tunneling magnetoresistance in epitaxial $Co_2MnSi/MgO/Co_2MnSi$ magnetic tunnel junctions by half-metallicity of Co_2MnSi and coherent tunneling, Appl. Phys. Lett. **101**, 132418 (2012).